Journal of Volcanology and Geothermal Research 325 (2016) 156–168

Contents lists available at ScienceDirect

Journal of Volcanology and Geothermal Research

journal homepage: www.elsevier.com/locate/jvolgeores

Physical and hydraulic properties of modern sinter deposits: El Tatio, Atacama

Carolina Munoz-Saez [a,b,*], Seth Saltiel [a,b], Michael Manga [a,b], Chinh Nguyen [c], Helge Gonnermann [c]

[a] University of California, Berkeley, California, USA
[b] Lawrence Berkeley National Lab, Berkeley, CA, United States
[c] Rice University, Houston, TX, United States

ARTICLE INFO

Article history:
Received 16 February 2016
Received in revised form 14 June 2016
Accepted 30 June 2016
Available online 04 July 2016

Keywords:
Silica sinter
Geothermal
Seismic velocity
Permeability
Porosity
Microbe filaments

ABSTRACT

Sinters are siliceous, sedimentary deposits that form in geothermal areas. Formation occurs in two steps. Hot water circulates in the subsurface and dissolves silica from the host rock, usually rhyolites. Silica then precipitates after hot water is discharged and cools. Extensive sinter formations are linked to up-flow areas of fluids originating from high temperature (>175 °C) deep reservoirs. Fluid geochemistry, microbial communities, and environmental conditions of deposition determine the texture of sinter and pore framework. Porosity strongly influences physical and hydraulic properties of rocks. To better understand the properties controlling the transport of fluids, and interpret geophysical observations in geothermal systems, we studied 17 samples of modern geyserite sinter deposits (<10 ka) from the active El Tatio geothermal field in northern Chile. We measured the physical properties (hydraulic, seismic, and electrical), and internal microstructure (using μX-Ray computed tomography). We find that the pore structure, and thus hydraulic and physical properties, is controlled by the distribution of microbial matter. Based on velocity-porosity relationships, permeability-porosity scaling, and image analysis of the 3D pore structure; we find that the physical and hydraulic properties of sinter more closely resemble those of vesicular volcanic rocks and other material formed by precipitation in geothermal settings (i.e., travertine) than clastic sedimentary rocks.

1. Introduction

Sinters are terrestrial, siliceous, sedimentary deposits that are common in geothermal areas with near-neutral alkali chloride springs and typically originate from deep reservoirs with temperatures >175 °C (Fournier and Rowe, 1966). Silica can be also deposited from acid-sulfate-chloride waters (e.g. Jones et al., 2000; Mountain et al., 2003; Rodgers et al., 2004; Schinteie et al., 2007). Sinter deposits are located at the surface of geothermal systems; near-vent deposits called geyserite form a thin unit that can reach up to ~15 m thicknesses, while the thickness of sinter terraces and aprons varies from 10 to 100 m (e.g., Campbell et al., 2015a).

Geophysical methods commonly used to image geothermal settings include seismic, electrical, and radar and hence require knowledge of the seismic velocity, density, and electrical conductivity of sinter to interpret geophysical data. Few studies report physical properties of sinter (e.g., Herdianita et al., 2000; Rodgers et al., 2004; Lynne et al., 2005, 2008), none of which report geophysical properties.

Physical and hydraulic properties of rocks are strongly influenced by their porosity and pore structure. The origin and evolution of sinter porosity have received more attention in the literature; primary porosity can be modified by post-depositional events including burial, compaction, secondary fluid circulation and precipitation of silica in pores, diagenetic transformation of silica, and dissolution via acid steam condensate (e.g., Fernandez-Turiel et al., 2005; Campbell et al., 2015b; Lynne et al., 2008). The evolution of porosity in some cases appears to be independent of mineral maturity (Lynne et al., 2005, 2008). The shape and size of the pores/voids preserved in the sinter layers provide information about the regime of water discharge in channels (Lynne, 2012). Primary porosity in microbial textures occurs in the matrix and inside silicified organisms (Jones and Renaut, 1997; Fernandez-Turiel et al., 2005; Campbell et al., 2015b). Abundant fenestral porosity has been observed in laminae and palisade micro textures (e.g., Konhauser et al., 2001; Fernandez-Turiel et al., 2005). Gas bubbles (<15 mm) released by photosynthetic bacteria can be trapped in microbial mats prior to silicification of microbes (e.g., White et al., 1964; Hinman and

* Corresponding author at: University of California, Berkeley, California, USA.
E-mail address: carolimunoz@berkeley.edu (C. Munoz-Saez).

http://dx.doi.org/10.1016/j.jvolgeores.2016.06.026
0377-0273/

Lindstrom, 1996; Lynne, 2012). Microbes can overgrow surfaces faster than the deposition rate of silica and produce macro-scale sinter textures of multiple curved laminations with oval or lenticular voids (Lynne, 2012).

To better understand the properties of modern sinter, interpret geophysical surveys and to provide estimates of properties that control the transport of fluids, we analyzed a set of young sinter samples from an active geothermal field located in north of Chile called El Tatio. We sampled proximal to middle facies of modern sinter deposits, and we examined the microstructure, porosity and distribution of microbial filaments in the samples by using optical (thin sections) and μX-Ray Computed Tomography methods. We measured the hydraulic, seismic, and electrical properties of the samples in the laboratory, and compared the measured relation between microstructure and physical properties with commonly used effective medium models and empirical relationships.

2. Importance of studying sinter

Depending on the distance from the geothermal vent and the flow regime, proximal, middle and distal deposits have distinctive sinter facies, including cones, mounds, channels, terraces, aprons, and marsh (e.g., Cady and Farmer, 1996; Braunstein and Lowe, 2001; Campbell et al., 2015a). Geyserite is a type of proximal sinter deposit characterized by dense and fine lamination that is generated by intermittent discharge from hydrothermal vents (White et al., 1964). Proximal deposits are associated with high temperature water, ranging from 75 to 100 °C (e.g., White et al., 1964; Walter, 1976a; Campbell et al., 2015a). Sinter, especially proximal deposits, provides a guide for identifying ore epithermal deposits and geothermal systems, These deposits indicate the location of up flow zones, and the position of vents/fractures connected to deep geothermal reservoirs (e.g., Sillitoe, 1993, 2015; Guido and Campbell, 2009; Lynne, 2012).

Sinter textures preserve information about the fluid geochemistry, discharge, microbial communities, and environmental conditions of deposition (e.g., Walter, 1976a, 1976b; Cady and Farmer, 1996; Hinman and Lindstrom, 1996; Konhauser and Ferris, 1996; Jones and Renaut, 1997, 2004; Campbell et al., 2001; Konhauser et al., 2001; Lowe et al., 2001; Jones et al., 2003; Guidry and Chafetz, 2003; Lynne and Campbell, 2003; Handley et al., 2005; Schinteie et al., 2007; Nicolau et al., 2014). Hot springs settings are inhabited by microbial communities; hence studying sinter can provide insights into the development of early life on Earth under extreme environmental conditions (e.g., Walter, 1972; Konhauser et al., 2003; Westall et al., 2015). Opaline silica deposits have been identified on Mars (e.g., Squyres et al., 2008; Ruff et al., 2011), and they are of astrobiological interest because terrestrial opaline sinters preserve signatures of microbial life. Microbial textures tend to remain longer than microfossils as fingerprints of organisms, which tend to disappear in ancient sinters (e.g., Guidry and Chafetz, 2003; Lynne et al., 2005). A few pre-Quaternary sinters with microbial fossils have been found in the geological record e.g., Devonian Drummond in Australia (e.g., Walter et al., 1996), Devonian Rhynie cherts in Scotland (e.g., Rice et al., 2002), Late Jurassic Deseado Massif in Argentina (Guido and Campbell, 2014; Campbell et al., 2015a).

Palisade texture is commonly preserved in the geological record, and it is associated with low-temperature (<40 °C) relatively calm water that accumulates in shallow terraces, large pools and distal apron-slope (e.g., Weed, 1889; Walter et al., 1996; Cassie, 1989; Cady and Farmer, 1996; Lynne and Campbell, 2003; Guido and Campbell, 2014; Campbell et al., 2015b). Palisade texture typically has thin laminated layers (1–5 mm thick) that are rich in microbial filaments; these layers alternate with solid silica horizons (e.g., Campbell et al., 2001, 2015b). Filaments arrange into closely packed, vertically-oriented, micropillar structures (e.g., Cassie, 1989; Cady and Farmer, 1996; Lynne and Campbell, 2003). Silicified stacks of filamentous palisade layers can form stromatolitic structures (e.g., Campbell et al., 2001, 2015b). These microbial filaments commonly correspond to photosynthetic cyanobacterias of the genus *Calothrix spp.*, which are characterized by individual filaments of >10 μm diameter and 4 mm length (Watanabe and Kurogi, 1975). Microbial filaments form felted mats. Mid-temperature (~40-60 °C) hot spring aprons and discharge channels are inhabited by thin <5 μm diameter sheathed filamentous cyanobacteria *Leptolyngbya ssp.* (e.g., Walter, 1976a; Cady and Farmer, 1996; Lowe et al., 2001). High-temperature (60–75 °C) proximal slopes and channels are inhabited by filamentous microbes of <1 μm diameter, which are in the limit of photosynthetic bacteria (Pierson and Castenholz, 1974). In near vent environments (>75 °C), sinter is deposited under subaqueous conditions and intermittently wetted by splash, waves, surging, or airborne eruptions (e.g., Lowe et al., 2001; Lynne, 2012). Biofilms of non-photosynthetic bacteria and archaea have been recognized in alkaline waters >75 °C (e.g., Bott and Brock, 1969; Huber et al., 1998; Blank et al., 2002; Cady, 2008).

Studying the properties of modern sinters offers insights to discriminate between depositional processes and later overprints. Mineralogical and textural changes in sinter occur gradually over time as a result of burial and diagenesis (e.g., Cady and Farmer, 1996; Herdianita et al., 2000; Lynne et al., 2012). However sinter diagenesis is mostly controlled by burial, circulation of secondary fluids and condensation of acid steam (e.g., Lynne and Campbell, 2003; Lynne et al., 2005, 2008). The main phase in fresh sinter is non-crystalline opal A, a hydrated amorphous form of silica. Micro-spheres of opal-A progressively change to nanospheres of opal-A/CT, lose water and crystallize to para-crystalline opal-CT, opal-C, and eventually to quartz (e.g., Chaika and Dvorkin, 1997; Herdianita et al., 2000; Rodgers and Cressey, 2001; Lynne et al., 2008).

3. El Tatio: Geological setting and characteristics of sinter deposits

El Tatio is an active geothermal area located in the Atacama Desert, northern Chile (elevation >4000 m). The heat of the system is provided by Holocene dominantly andesitic stratovolcanoes with no historical local eruptions (Lahsen, 1976a, 1976b). Based on chemical and isotopic characteristics, the thermal waters are inferred to originate from mixing between magmatic, meteoric and hydrothermal sources (Cusicanqui et al., 1976; Giggenbach, 1978; Cortecci et al., 2005; Tassi et al., 2010). The thermal water has pH from 6 to 8, conductivity of ~20 mS/cm, high concentrations of Cl^- (>6000 mg/l), Na^+ (>3500 mg/l), SiO_2 (>220 mg/l), and As^{3-}(>30 mg/l), and low SO^{4-} (<50 mg/l) (e.g., Cusicanqui et al., 1976; Giggenbach, 1978; Fernandez-Turiel et al., 2005; Cortecci et al., 2005 ; Tassi et al., 2010; Nicolau et al., 2014).

Most thermal manifestations are located in an area ~ 10 km^2, and the distribution of the thermal features is bounded by a N—S trending half-graben (Fig. 1). The basin is filled with ~1000 m of sub-horizontal ignimbrites, tuffs and lavas and covered by Holocene alluvial, glacial (Healy, 1974; Lahsen and Trujillo, 1975) and sinter deposits. Diverse thermal features have been reported, including geysers, springs, perpetual spouters, mud pools, mud volcanoes, and fumaroles (Glennon and Pfaff, 2003). Sinter deposits form an array of mounds, geyser cones, pool-rim dams, and complex sinter aprons characterized by shallow terraced pools (Jones and Renaut, 1997). The absolute age of the sinter deposits is unknown, a bound of <10 ka can be constrained by the time of the last glacier retreat considering the glacial deposits below the sinter units (Lahsen, 1976ab). However, considering the rates of silica precipitation and the size of the deposit, deposition would likely have begun ~1 to 4 ka (Nicolau et al., 2014).

A precipitation rate of silica between 1.3 and 3.4 kg/m^2 per year was measured in-situ for sub-aerial sinter that accumulated during 10 months along different portions of the discharge channel of a hot spring (Nicolau et al., 2014). This rate is lower than in Waiotapu, New Zealand, where the sub-aerial precipitation is 1 to 10 kg/m^2 (Handley et al., 2005), but relatively high considering that the silica content of

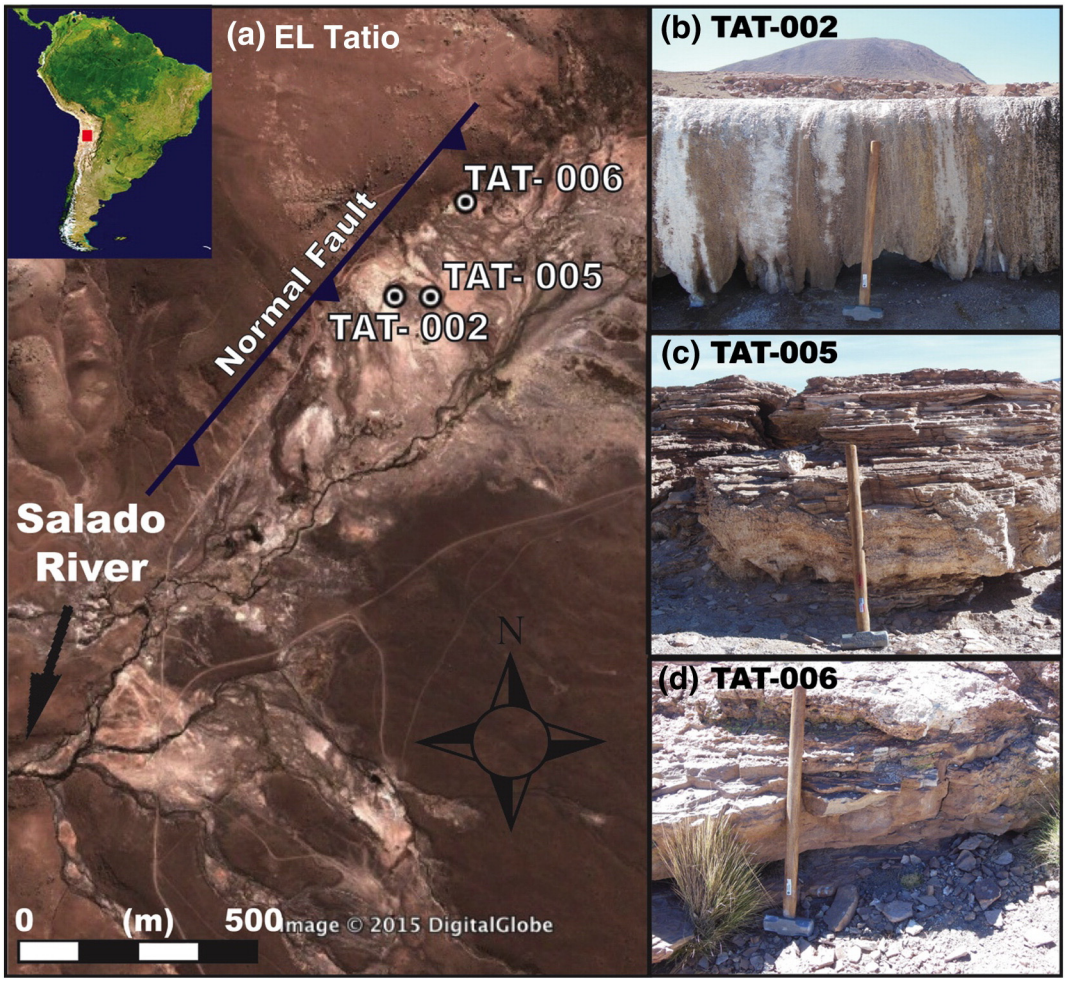

Fig. 1. El Tatio Geyser Field: (a) Location on Google Earth (imagery date: 5/17/11); the blue line indicates the normal fault that bounds the El Tatio half-graben and the dots indicate the sampled sites: (b) TAT-002 sinter terrace ($22_o19'52.09"S/68_o0'39.47"W$), (c) TAT-005 extinct cone/mound without signs of geothermal activity ($22_o19'30"S/68_o0'36.36"W$), and (d) TAT-006 extinct cone/mound expelling vapor ($22_o19'44.9"S/68_o0'32.81"W$). The length of the hammer in the images is 0.9m.

the water in the measured springs of El Tatio (147 ppm) is lower than in Waiotapu (430 ppm). Silica deposition is governed by environmental conditions leading to high evaporation rate and high cooling rate (Nicolau et al., 2014).

Previous studies of sinter at El Tatio explained some petrographic, chemical, and textural characteristic of sinter, describing opal-A as the dominant silica phase, with halite and gypsum as accessory minerals (e.g., Jones and Renaut, 1997; Rodgers et al., 2002; Glennon and Pfaff, 2003; Fernandez-Turiel et al., 2005; Garcia-Valles et al., 2008; Lynne, 2012; Nicolau et al., 2014). Mineralogically mature opal-C is mostly located in older distal depositional environments and near active fumaroles (Garcia-Valles et al., 2008). Sinter deposits preserve microbial communities of cyanobacteria, green bacteria, diatoms, and particles of silicified pollen and plants in their layering (Fernandez-Turiel et al., 2005; Garcia-Valles et al., 2008; Nicolau et al., 2014). The high elevation of El Tatio lowers the boiling point of water to ~86.4 °C, and leads to higher UV radiation than at other sinter areas, e.g., Yellowstone in the USA, hot springs in New Zealand and Iceland. Precipitation of silica offers cyanobacteria protection against UV radiation (Phoenix et al., 2006). Compared to low the altitude hot springs in New Zealand, the El Tatio microbial mats have similar color and texture, but slightly higher temperatures (Lynne et al., 2012). Proximal to geysers (70 to 86 °C) are green bacteria that were observed at Yellowstone in waters below 75 °C (Fernandez-Turiel et al., 2005). Ranges of temperature for hyperthermic and mid-temperature microbes at El Tatio were not strictly defined (e.g., Phoenix et al., 2006; Nicolau et al., 2014). Hyperthermophilic bacteria (1 μm diameter) and mid-temperature microbes (>5 μm diameter) coexist with boiling-related textures and proximal environments of >60 °C (Nicolau et al., 2014). Filamentous cyanobacteria *Lyngbya ssp.* (<5 μm diameter), *Calothrix ssp.* (>10 μm diameter), and *Phormidium ssp.* (2-12 μm diameter), were identified from microbial mats collected in outflow channels and terraces of <40 °C (Phoenix et al., 2006).

At El Tatio, geysers and spouting springs discharge from tube-shaped vents that can be surrounded by steep-sided mounds or cones up to ~3 m high and ~3 m in basal diameter, or by pools (few cm up to 5 m diameter) filled with hot water, and bounded by pool-rim dams (Jones and Renaut, 1997). Deposits present irregular shapes and discontinuous laminations, smooth knobs and ridges, columns, erected spicules, and oncoids (Jones and Renaut, 1997; Fernandez-Turiel et al., 2005; Garcia-Valles et al., 2008; Nicolau et al., 2014). Strong daily variations in temperatures produced freezing-related textures: platelets, micro columns and ridges (Nicolau et al., 2014). Microscopically, silica spheres can be randomly aggregated forming layers or botryoidal crusts; massive silica forms smooth-dense layers; and biogenic silica forms porous sinter laminations (Fernandez-Turiel et al., 2005; Garcia-Valles et al., 2008; Nicolau et al., 2014). Middle facies associated with discharge channels, elevated sinter terraces around springs and geysers, and mid-apron have macro-scale textures characterized by laminated spicules and oncoids of varied shape (Jones and Renaut, 1997; Fernandez-Turiel et al., 2005; Garcia-Valles et al., 2008). Micro-

scale textures show fine laminations alternating with palisade textures (Jones and Renaut, 1997; Fernandez-Turiel et al., 2005).

4. Methodology

We collected samples from three locations: TAT-002, TAT-005 and TAT-006 (Fig. 1). TAT-002 is a sinter terrace formed by the discharge of an active geyser located 5 m from the sample site. This sample was still saturated with water, and the temperature was ~40 °C when collected. TAT-005 and TAT-006 are abandoned geyser cones, and samples were dry. TAT-005 is located in an area without discharge of thermal fluids, while at TAT-006 vapor was still emanating from the center of the cone. Cores derived from samples collected from different stratigraphic levels were sampled systematically from the bottom of the cone to the top every 5 to 10 cm, and labeled alphabetically in the same order. We assume that samples from the bottom were older than samples from the top. Measurements were performed only in samples of fine-layered sinter (1 to 5 mm laminations).

For the petrography, we analyzed thin sections of the three sampled sites with a petrographic microscope. We analyzed 2.5 mm diameter cores from sample TAT-002 with μX-ray computed micro-tomography (μXRT), which is a non-destructive technique that creates a high-resolution three-dimensional image of rock density (resolution of 1.3 μm/voxel). μXRT was performed at the Advanced Light Source (ALS) beamline 8.3.2, Lawrence Berkeley National Laboratory (LBNL). We used 22 keV monochromatic X-rays. We reconstructed and visualized the 3-D internal structure of the sample using Octopus, Image-J and Avizo software.

For X-ray diffraction (XRD), considering that sinter diagenesis can be patchy spatially and layers can be heterogeneous in composition, we powdered different sinter layers from the hand sample, mixed them and analyzed a few milligrams. We used a PANalytical X'Pert Pro diffractometer equipped with a Co X-ray tube and a fast X'Celerator detector. Minerals produce characteristic X-ray patterns that can be compared with a database of known phases using the analytical software XPERT-PRO.

For hydraulic, seismic and electrical properties analysis, we drilled 17 cores 2.5 cm in diameter. Some of the cores were perpendicular, and others orthogonal, to the lamination. The connected porosity was determined in the lab using a Micromeritics AccuPyc II 1340 (Nguyen et al., 2014) that measures the change of helium pressure within the calibrated volume and Boyle's law. Powdered samples were also measured using the AccuPyc II 1340© to determine the density of the skeleton (solid plus any isolated vesicles that are not somehow connected to the sample surface). We computed the total porosity by dividing the difference between the volume of skeleton and the volume of the cylindrical core by the total volume of the core. Bulk density of the core was determined from the ratio between the total mass and volume of the core.

For Darcian permeability measurements we used a Capillary Flow Porometer (Model CFP-1100AXL-AC, Porous Media, Inc.). We jacketed the cores with impermeable epoxy resin, except at the two flat ends. The inlet air pressure varied from $1.1x10^5$ Pa up to $6x10^5$ Pa while the outlet pressure was atmospheric. We measured each sample with 2–3 interchangeable flow meters to improve accuracy. The pressure gradient across the sample length varied between 0 and $5x10^5$ Pa m^{-1}, and the measured volumetric flow rate of air was between 3×10^{-3} and 5×10^{-7} m^3 s^{-1}, with an accuracy ~5×10^{-8} m^3 s^{-1} (~1% of the minimum measured flow rate).

For the measurement of seismic velocities we used ultrasonic waves. We used Source/Receiver NER P and S wave transducers and an oscilloscope, Tektronix TDS 210. A sonic pulse is generated at one side of the

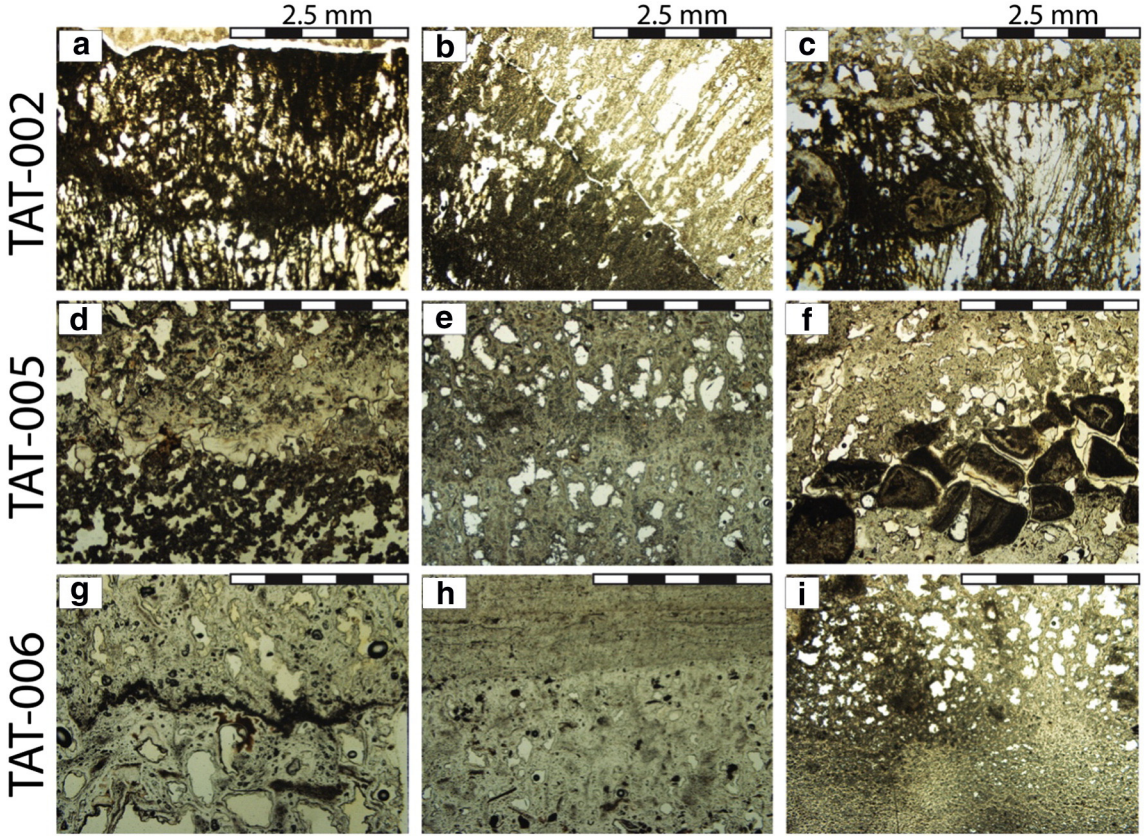

Fig. 2. Thin sections imaged with transmitted light showing different sinter layers. (a), (b), and (c) show variation within the same palisade texture from sample TAT-002. (d) TAT-005D, (e) TAT-005G, and (f) TAT—005I, represent different levels of the cone at site TAT-005. (g) and (h) are thin sections of sample TAT—006H, and (i) is a thin sections of TAT-006Q. The scale bar at the top of the images is the same for all images (2.5 mm).

sample and we measure the arrival time of the wave in the other end of the sample. We obtained the acoustic velocities by measuring the travel time (minus the 'face to face' time in the transducers themselves) along the sample axis divided by the sample length. When the signal exceeded a threshold, we manually selected this point as the arrival time of the wave. We calculate P-wave velocity (V_P) in dry and saturated samples, given that the deposition of the sinter occurs in an aqueous environment, and the pore space in geothermal reservoirs is saturated. Saturation also minimizes the effect of small cracks in the rocks that may affect the measurements. We used two methods to saturate the sample: vacuum chamber and boiling; we obtained >80% of saturation in every sample. *S*-wave velocity (V_S) was only measured in dry samples, since the fluid should not affect the shear modulus of the samples. To test the anisotropy of the samples, we measured the S-wave velocity in two perpendicular directions of polarization. For V_P and V_S we used MHz frequencies, and the error in velocity is <3%. Some samples were too attenuating at these frequencies to make an accurate measurement; they were excluded from this study. The elastic moduli of the rocks were calculated with the seismic velocities and the bulk density of the samples. There are no laboratory standards for the seismic properties of opal-A in sinter rocks in the literature. As a reference, we used standard values of opal measured in the lab on marine chalks with opal-A as the main mineral phase, and <50% of opal A/CT (Chaika and Dvorkin, 1997; Chaika, 1998).

We measured the electrical resistance of the saturated samples by connecting an electrode to each end of the core and applying an oscillating electrical current. The resistivity was calculated by measuring the voltage across the sample of a measured length, given the applied current with a range of frequencies from 0.1 to 1000 Hz. The measured resistivity varied at the lower frequencies (due to surface conduction effects) but became constant at higher frequencies; we report the latter value. We used an IET RS-200 W, with an accuracy, after subtracting the residual impedance, of ~0.2%. We measured the resistivity of the samples saturated (R_{rock}) with two brines of different resistivity, $R_{w1} = 41.35\ \Omega m$, $R_{w2} = 15.81\ \Omega m$. We expected the lower resistivity of the second brine to lessen the effect of partial saturation because aqueous conduction should dominate over mineral surface conduction, which is more sensitive to saturation. Also the resistivity of R_{w2} is close to the corresponding values of conductivity and salinity of water reported in the field (e.g., Giggenbach, 1978; Cortecci et al., 2005). The resistivity of the brines was used to determine the resistivity index or formation factor (F_R) that corresponds to the ratio between the resistivity of the saturated sample and the resistivity of the water saturating the rock ($F_R = R_{rock}/R_{water}$) (Archie, 1942).

5. Results

5.1. Observations of sinter layers and pores structure

In thin sections, we observe that El Tatio samples are composed of diverse silica layers, with a variable pore concentration, size, and shape (Fig. 2). Sample TAT-002 has a palisade texture, with elongated pores perpendicular to the lamination (Fig. 2abc). In older cones (TAT-005 and TAT-006), we observe palisade-like textures, with a similar orientation of the pores, but they have a smaller amount of voids, and these voids are much more rounded (Fig. 2eg). We find layers of different textures, including palisade-like textures (Fig. 2e), massive silica (Fig. 2h), and porous silica (Fig. 2di). The boundaries between layers vary: in places we observe sharp changes in texture (Fig. 2dh) and in others we find transitional changes (Fig. 2bi). Dark lines delimit different layers (e.g., Fig. 2g), and fragments of volcanic rocks or glass shards (Fig. 2f) were deposited between layers. Fragments of sub-angular glass shards provide evidence of subaerial exposure between depositional periods, evidence of geyser quiescence.

We find filamentous microbes in the palisade texture described above for the young sample TAT-002. From the thin sections and 3D reconstructions from μX-ray computed tomography (Fig. 3), we observe that filaments have diameters ~10 μm. Filaments tend to be oriented perpendicular to the lamination. Some filaments are long and cross through the entire core diameter (2.5 mm). The pores are also elongated

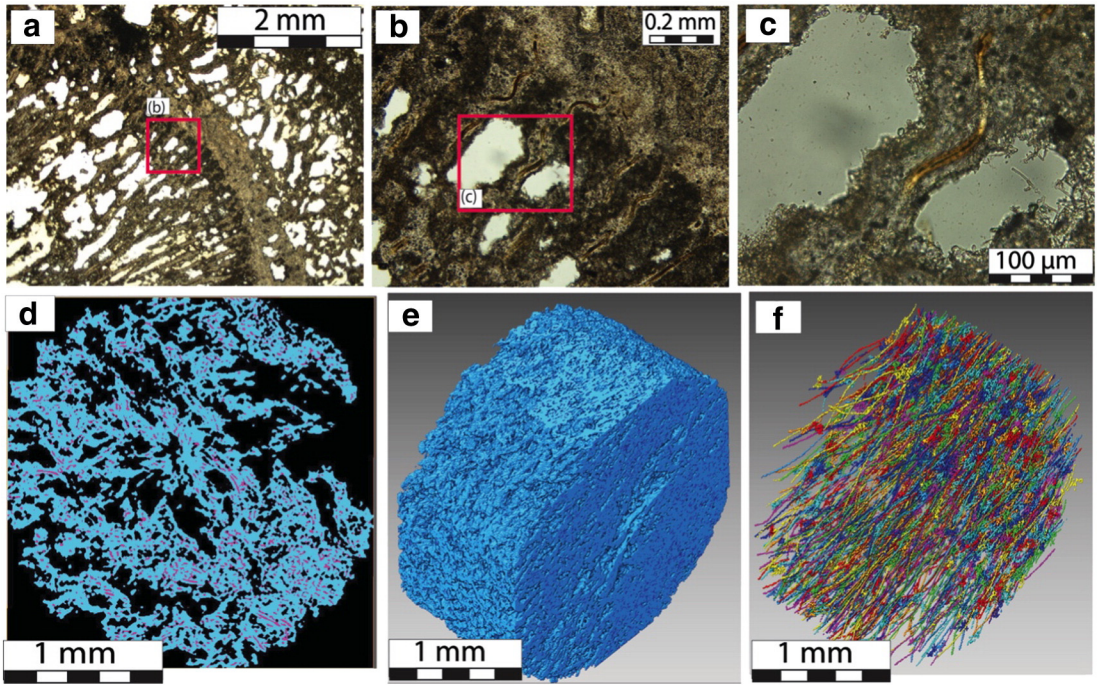

Fig. 3. Sample TAT-002, thin sections and XRay Tomography reconstrutions (XRT): (a) Thin section showing palisade texture with elongated pores perpendicular to the layering (Fig. 2c). (b) Magnification of (a) showing elongated microbial filaments between pores, magnified further in (c). (d) One slice through the XRT image of the rock; black background shows empty space (pores), light blue identifies solid matrix and pink shows the microbe filaments. (e) 3D reconstruction of the core including filaments. (f) 3D reconstruction of filaments, separated from the solid matrix (light blue in d). The image exaggerates the diameter of the filaments by a factor of 4.

in the same direction as the filaments. Using our 3D image volumes, we calculate that the filamentous bacteria surpass 20% of the volume of the rock.

Additionally, in the older samples we observe oncoid structures of ~2 mm diameter, surrounded by porous silica (TAT—005I, Fig. 4a). Oncoids have concentric massive layers of silica, while the surrounding porous silica have a palisade texture. The dark regions around the pores can be attributed to microbial filaments. In sample TAT-006Q we find wavy laminated textures (Fig. 4b) with fenestral porosity between the laminae. From detailed observations inside the pores of sample TAT—006H, we can establish that glassy silica precipitated from the border to the center of the pores (Fig. 4c). Crystals of hornblende ($Ca_2(Mg, Fe, Al)_5(Al, Si)_8O_{22}(OH)_2$) infill pores (Fig. 4d).

XRD from different levels of TAT-006 (Fig. 4e) indicate the predominance of non-crystalline opal-A, and the peaks show the presence of detritial accessory minerals. TAT-006 A present several small diffraction peaks, the one at 31° is associated with quartz (SiO_2), and the one at 32.7° with plagioclase, probably albite ($Na(Si_3Al)O_8$). TAT-006I shows diffraction peaks at 25.6° and 33.3° from cristobalite (polymorph of quartz), 31° and 42.9° from quartz, and 32.5° and 32.7° from plagioclase. TAT-006 M has the same peaks for cristobalite, quartz, plagioclase, and peaks at 31.5° and 41.6° from zircon ($ZrSiO_4$).

Using μXRT-3D image analysis (Fig. 5), we estimate that the porosity varies among cores from ~20% to 50%, with slightly lower values for the smaller cores because we did not sample the larger voids. The size distribution analysis of individual pores (diameter > 5 μm) show that more 85% of the pores had a volume < 10^5 μm^3, but their contribution to the total porosity is <5%. Pores with volume between 10^5 and 10^6 μm^3 account for ~10% of the pores, and ~15% of the total porosity. The rest of the pores with volume > 10^6 μm^3 correspond to 0.5% of the number of pores and ~80% of the total porosity.

5.2. Hydraulic, seismic, and electrical properties

Table 1 summarizes the measurements of bulk density (ρ), porosity (ϕ), permeability (k), seismic velocities (V_P and V_S) and formation resistivity factor (F_R) of the sinter samples. The propagation velocities of *P*-waves in dry and saturated samples are denoted V_{PDry} and V_{PSat}, respectively. The two polarization directions of *S*-waves are denoted as V_{S1} and V_{S2}. The formation resistivity factors (F_{R1} and F_{R2}) were measured with two brines. The cores are also labeled according to whether they were oriented parallel (//) or orthogonal (⊥) to the lamination.

5.2.1. Relationships between porosity (ϕ) and permeability (k)

The total porosity (ϕ_{Tot}) ranges between 25.8 and 54.1%, and the mean porosity is 39.4%, with most of the porosity connected (ϕ_{Conn}) (Fig. 6a). The values of permeability (k) range between 10^{-15} to 10^{-12} m^2, with a mean k of 10^{-13} m^2 (Fig. 6b), showing a slight positive correlation with porosity. The highest value of k was measured in a core parallel to the layering (TAT-006LC). Some samples were cored parallel and perpendicular to the layering. k in the parallel cores was 1 to 2 orders of magnitude higher (TAT-006I and TAT-006 L) than in the orthogonal cores. In other samples, two orthogonal cores were analyzed, and k varied up to 2 orders of magnitude (TAT-006 M) (Table 1).

5.2.2. Anisotropy of S-wave propagation (V_S)

We analyzed the anisotropy of S-wave velocity with the ratio V_{S1}/V_{S2}, where the faster direction is 1 such that the ratio was always greater than or equal to 1 (Fig. 7a). For samples oriented parallel to the lamination, the two polarizations were different relative to the layering. High V_{S1}/V_{S2} indicates that the layers have different seismic properties, or are seismically anisotropic. For orthogonal samples, both polarizations sample the same layers. High V_{S1}/V_{S2} suggests that the layers themselves are anisotropic. For most of the samples V_{S1}/V_{S2} is close to 1, indicating that most of the samples are isotropic. For those samples where V_{S1}/V_{S2} is far from 1, there is no clear relationship with respect to orientation of the samples.

5.2.3. Relationships between seismic velocities V_P, V_S, porosity (ϕ), and bulk density (ρ)

Seismic velocities show large scatter, with low to medium coefficients of correlation in typical linear empirical relationships (Fig. 7bcde). This may be due to highly compliant open cracks or grain boundaries (Mavko et al., 1998), which are more prevalent in some of the samples.

P-wave velocities measured in dry samples (V_{PDry}) are more variable than water-saturated samples, and V_{PSat} shows a better correlation coefficient with total porosity (ϕ) (Fig. 7b). *S*-wave velocities show large scatter, and poor correlation with total porosity (ϕ) (Fig. 7c). The relation between the seismic velocities in dry samples, V_{PDry} and V_S (Fig. 7d), show a moderate correlation. V_{PSat} and bulk density (ρ) are also moderately correlated (Fig. 7e).

5.2.4. Critical porosity (ϕ_C)

Most porous materials have a critical porosity (ϕ_C) that separates their behavior in two domains: (1) $\phi_{Tot} < \phi_C$ is the load-bearing domain

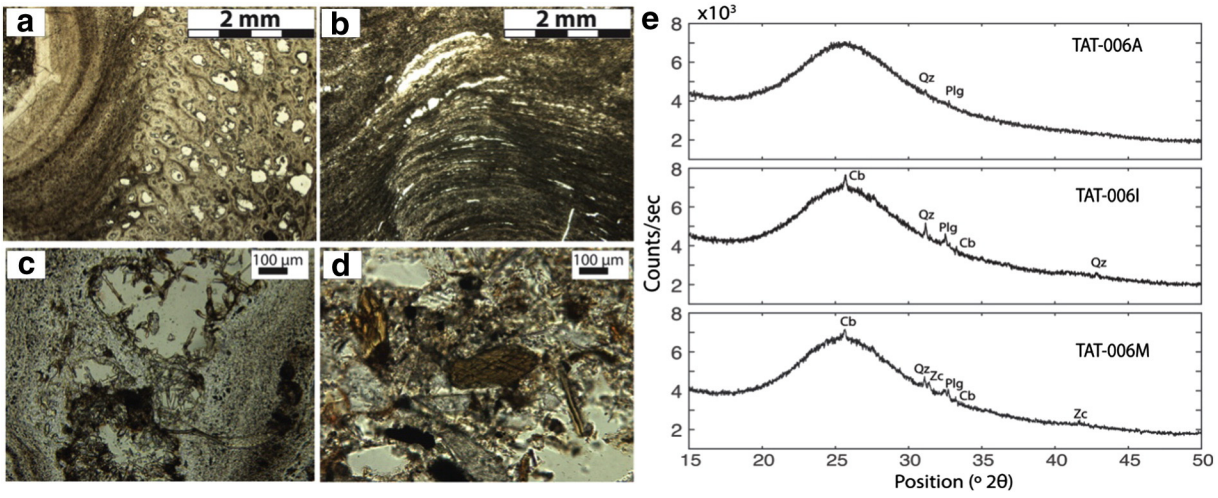

Fig. 4. Pore structure and XRD in older cones. (a) Sample TAT-005I shows a silica oncoid and porous silica around it forming palisade-like texture. (b) Sample TAT-006Q has wavy laminated structures with pore space between laminae. (c) TAT-006H shows details of silica filling pores from the border to the center of the pores. (d) TAT-006H shows the accessory mineral hornblende filling the pores. (e) XRD diffraction of three different samples from cone TAT006 (TAT-006A was the bottom of the cone, TAT-006I was ~0.5 m height, and TAT-006M was ~1 m height from the bottom of the cone). XRD traces show opal-A broadbands, and accessory crystals of cristobalite (Cb), quartz (Qz), zircon (Zn), and plagioclase (Plg).

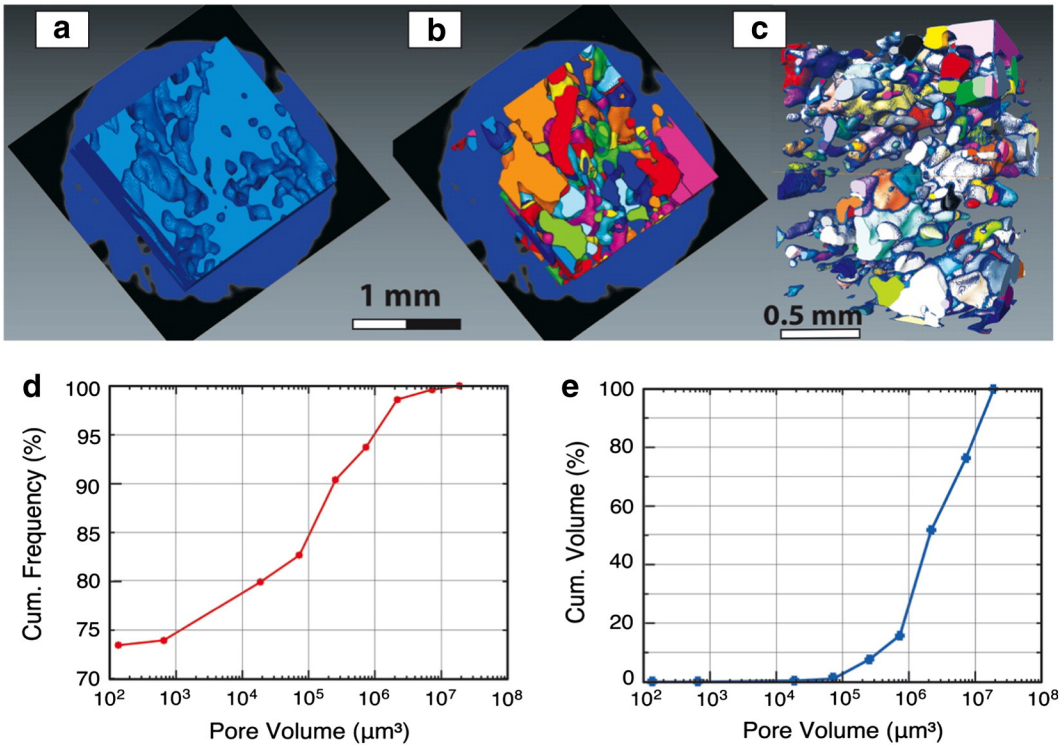

Fig. 5. 3D XRT reconstruction and pore size distribution of sample TAT-002. (a) 3D reconstruction of the rock and, (b) individual pores in the central part of the core; blue circle on top of black square corresponds to one slice of the XRT as a reference. (c) 3D view of individual pores. (d) Plot of cumulative frequency as a function of pore volume (e) Plot of cumulative volume as a function of pore volume.

where the solid supports the rock, (2) $\phi_{Tot} > \phi_C$ is the suspension domain, where the solids are in suspension. In the load-bearing domain, seismic velocities range between the mineral (zero porosity) and the suspension value at ϕ_C, and this dependence can be characterized by the relationship between ρV^2 and ϕ (Nur et al., 1991, 1995, 1998). From our sinter samples, we estimated ϕ_C~71% (Fig. 8a). When $\phi_0 = 0$, the values ρV_P^2 and ρV_S^2 correspond to the elastic moduli of the mineral: *P*-wave modulus (M) and *S*-wave or shear modulus (G), respectively. From the linear regression of ρV_{PSat}^2 vs. ϕ_{Tot}, we obtain that M is 41.6 GPa for the saturated rock and 34.5 GPa for the dry rock, and G is 13.6 GPa. Given the great scatter of the seismic velocities, the values of M and G have large uncertainties.

5.2.5. Effective medium model and the effects of inclusion shape

Effective medium models describe the macroscopic properties, such as elastic moduli, of a solid with inclusions of a different phase. Through a self-consistent approximation, the model uses the analytical solution for a single inclusion, then iteratively solves for the moduli of the background mixture, incorporating interactions between inclusions (O'Connell and Budiansky, 1974). The model of Kuster and Toksoz

Table 1
Summary of the laboratory measurements: bulk density (ρ), porosity (ϕ_{Tot} and ϕ_{Conn}), permeability (k), *P*-wave velocity (V_{PDry} and V_{PSat}), *S*-wave velocity (V_{S1} and V_{S2}), and formation resistivity factor (F_{R1} and F_{R2}). We added the core orientation, parallel (//) or orthogonal (⊥), and type of petrographic analysis: thin section (TS), X-ray diffraction, and µX-ray tomography (µXRT).

Sample	ρ (g/cm^3)	ϕ_{Tot} (%)	ϕ_{Conn} (%)	k (m^2)	V_{PDry} (km/s)	V_{PSat} (km/s)	V_{S1} (km/s)	V_{S2} (km/s)	F_{R1} (Ωm)	F_{R2} (Ωm)	Or	TS/ XRD/ µXRT
TAT-002	1.00	55.79	52.92	2.33E-13	2.57	2.73	1.87	1.39	1.02	1.26	//	TS µXRT
TAT-005D	1.48	32.90	30.49	1.12E-13	3.34	3.76	3.14	2.11	–	–	⊥	TS
TAT-005G	1.37	37.62	35.69	1.85E-15	3.35	3.54	2.45	2.51	–	–	⊥	TS
TAT-005H	1.15	47.95	46.50	7.46E-15	3.14	3.31	3.11	1.92	2.60	2.98	⊥	TS
TAT-005I	1.19	45.51	43.71	–	–	–	–	–		–	⊥	TS
TAT-006 A	1.63	25.78	25.17	6.89E-15	3.69	4.09	2.25	2.27	7.71	10.34	⊥	XRD
TAT-006B	1.41	35.32	34.36	1.97E-13	3.63	3.80	1.99	2.04	4.47	2.79	//	–
TAT-006FA	1.36	37.38	36.62	1.09E-12	3.62	3.74	2.17	1.92	9.81	3.47	⊥	–
TAT-006H	1.31	40.39	39.97	9.22E-14	2.63	3.77	1.51	1.19	16.61	4.48	⊥	TS
TAT-006IA	1.51	31.87	30.61	1.11E-14	3.06	3.84	2.09	2.00	5.611	10.98	⊥	XRD
TAT-006IB	1.53	31.13	29.79	4.26E-13	3.66	3.89	2.11	2.66	–	–	//	–
TAT-006LA	1.28	41.62	41.09	2.00E-14	3.35	3.38	2.42	2.35	6.48	3.58	⊥	–
TAT-006LB	1.18	46.25	46.28	3.14E-14	3.15	3.51	1.75	1.86	8.55	5.91	⊥	–
TAT-006LC	1.00	54.14	54.83	9.53E-12	3.48	3.48	2.02	1.94	15.70	5.01	//	–
TAT-006MA	1.26	43.62	42.72	6.99E-13	3.65	3.84	2.35	2.28	–	–	⊥	XRD
TAT-006 MB	1.31	41.34	39.56	6.30E-15	3.78	4.17	2.42	2.28	–	–	⊥	–
TAT-006Q	1.47	33.28	31.81	1.65E-13	4.13	4.14	2.57	2.48	17.79	7.38	//	TS
TAT-006RB	1.44	34.58	32.89	4.13E-14	4.00	4.09	3.58	2.14	1.02	8.08	//	XRD
Mean	**1.33**	**39.80**	**38.61**	**7.45E-13**	**3.43**	**3.71**	**2.34**	**2.08**				
Std	**0.18**	**8.06**	**8.33**	**2.28E-12**	**0.42**	**0.36**	**0.53**	**0.38**				

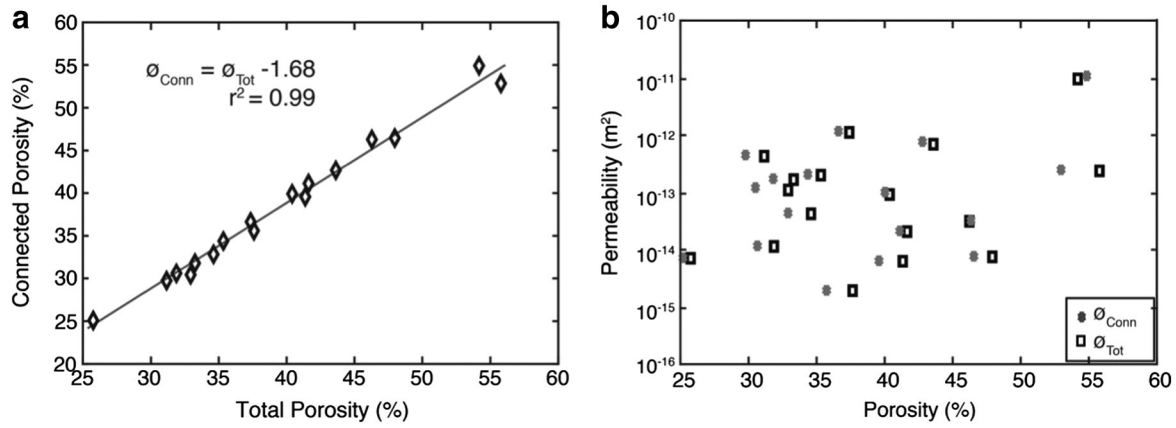

Fig. 6. Density, porosity and permeability. (a) Linear relationship between total porosity (ϕ_{Tot}) and connected porosity (ϕ_{Conn}). (b) Porosity (ϕ_{Conn} and ϕ_{Tot}) and permeability (k) show a weak relationship. Error bars are smaller than the plotted symbols.

(1974) uses this self-consistent approximation to calculate *VP* and *VS* for a range of porosities (density of inclusions) depending on the shape of the inclusions (Appendix A). We identify inclusions as pores filled with water. Using ellipsoidal penny-shaped cracks (Berryman, 1980), we estimate a range of possible of pore shapes (parameterized by aspect ratio α = semi-minor axis/semi-major axis) that fit our sinter data. We calculate the model considering the properties for the two extremes cases of minerals in sinter: opal and quartz (Fig. 8c, and Appendix A). For opal, the implied aspect ratio (α) ranges between 0.2 and 0.8. For quartz, the aspect ratio is lower and has a smaller range of possibilities (from 0.09 to 0.11).

5.2.6. Empirical relation between resistivity (F_R) and porosity (ϕ)

The formation factor is an intrinsic property of the rock (independent of the conductivity of the fluid), related to the efficiency of water-filled paths in conducting electrical currents through the medium. Electrical properties of a rock depend on the pore geometry and fluid distribution. Archie (1942) found an empirical power law relationship between the electrical properties (F_R), and the porosity (ϕ) of the rocks in sandstone reservoirs ($F_R = a\,\phi^{-m}$), where the m is the cementation exponent and is usually close to 2 for consolidated rocks, and a is the tortuosity factor generally close to 1, assuming fully saturated conditions. For the sinter, both measurements of F_R roughly show a power law relationship with porosity (Fig. 9). For the fit with the more resistive brine, the F_{R1}, the cementation exponent m is −1.9 and the tortuosity factor a is 0.71, while for the less resistive brine, F_{R2}, the fit of the exponent and factor increases to −2.44 and 0.79 respectively. Considering the data from both brines, the cementation exponent m is −2.16 and the tortuosity factor a is 0.75.

6. Discussion

In our samples, we observe silica around filamentous material forming palisade fabric, and porous and massive silica layers without biogenic components (Figs. 2, 3 and 4) similar to sinter textures described previously in El Tatio (Jones and Renaut, 1997; Fernandez-Turiel et al., 2005; Garcia-Valles et al., 2008; Nicolau et al., 2014). In sample TAT-002, we observe that silica and pores are elongated parallel to the bacteria (Fig. 3). Some levels of the older cones TAT-005 and TAT-006 preserve similar pore structures, even though direct evidence of bacteria are unclear (Figs. 2 and 4), probably due to the complete replacement of cellular material by silica (Westall et al., 1995, 2000). Similar pore frameworks have been described for palisade textures in low temperature environments and near vent-sinter (e.g., Lowe et al., 2001; Fernandez-Turiel et al., 2005; Campbell et al., 2001). We conjecture that bacterial filaments determine the pore structure in the rock, however the presence of biological material does not determine the origin of the silica precipitation. Microorganisms can provide a favorable substrate for opaline silica precipitation (e.g., Cady and Farmer, 1996; Jones and Renaut, 1996, 1997; Renaut et al., 1999). Thus silicification around microbial material produces a structural fabric that characterizes some sinter textures (Campbell et al., 2015ab). However, some studies indicate that silica precipitation is largely abiogenic due to cooling and evaporation (e.g., Walter, 1976a; Braunstein and Lowe, 2001; Guidry and Chafetz, 2003), and cyanobacterial surfaces have a negligible effect on silica nucleation (e.g., Yee et al., 2003; Benning et al., 2004; Handley et al., 2005). μX-Ray allow us to isolate and quantify the volume and shape of the silica matrix, bacterial material not replaced by silica, and isolated pores (Figs. 3 and 4). Sinter textures, including pore framework, can survive beyond fossilization, and can potentially be explored with this method.

Even though our measurements were restricted to the finer and most homogeneous sinter layers, we find that the physical properties and empirical relationships have large scatter. Observed microstructures show heterogeneities in different layers and within single layers, with respect to pore size and shape, and the extent to which pores have been infilled. The total porosity of our samples varied between 25 and 56%. Previous studies on young sinter, phase opal-A dominant, reported a similar porosity range of 10 to 60% for samples from New Zealand estimated to be <2 ka (Herdianita et al., 2000), and lower values <20% of porosity for samples from Opal Mouth, USA dated by ^{14}C at ~1.9 ka (Lynne et al., 2005), and <25% at Steamboat, USA, whose youngest ^{14}C age was ~6283 ± 60 years BP (Lynne et al., 2008). Even though, the absolute age of El Tatio samples is unknown, the youngest sample (TAT-002) has the highest porosity compared with the samples collected closest to the bottom of extinct cones (TAT-005D and TAT-006 A). The shape of the individual pores changed from elongated in the younger sample (TAT-002) to more rounded in the older samples (TAT-005 and TAT-006). There was no extensive evidence of dissolution, burial, compaction or diagenesis. For samples exposed longer at the surface, the reduction of porosity and shape change can be attributed to secondary precipitation of silica within the pores.

Petro-physical properties of the rocks depend on the lithology and the texture of the rock, including grain sorting and shape of voids (-Mavko et al., 1998). Bulk density of the rock (ρ) is closely related to porosity by $\rho = (1-\phi)\rho_o + \phi\rho_{fl}$, where ρ_o is the density of the mineral, and ρ_{fl} is the density of the fluid (water). Here we infer a mineral density of 2.18 g/cm^3. The measured density of opal-A particles in sinter range between 1.5 and 2.2 g/cm^3 (Herdianita et al., 2000; Lynne et al., 2005, 2008), and in chalk reached 2 g/cm^3 (Chaika, 1998). Denser accessory minerals like quartz (2.65 g/cm^3) and cristobalite (2.33 g/cm^3) (e.g., McSkimin et al., 1965; Mavko et al., 1998) could have slightly increased the bulk density, and the mineral density

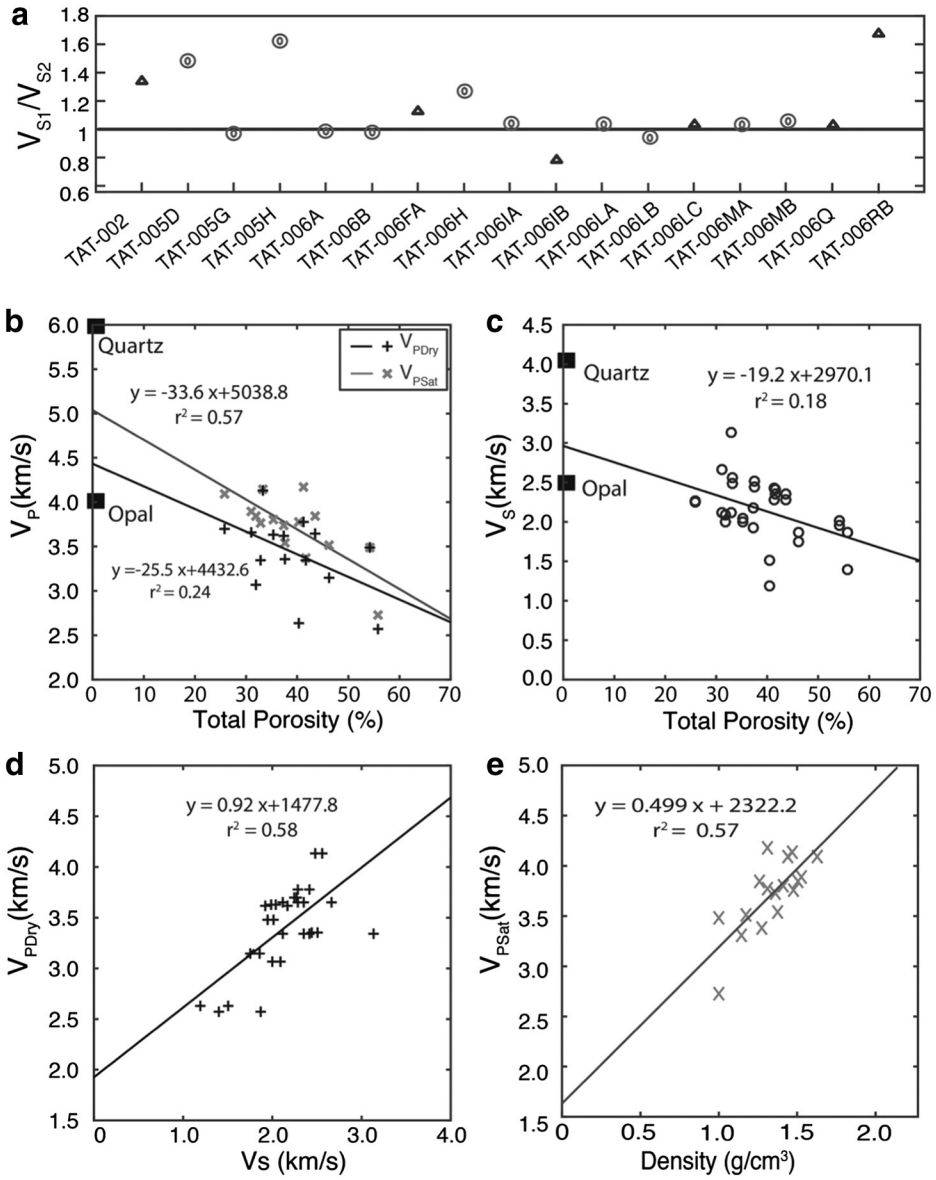

Fig. 7. Seismic velocities. (a) Anisotropy of S-wave propagation: x-axis shows the name of every sample, and the y-axis is the ratio between the two polarized velocities. The triangles correspond to samples that were measured parallel to the layering and circles are samples perpendicular to the layering. V_{S1}/V_{S2} close to 1 indicate that waves are propagating in isotopic layers. (b) P-velocities (V_{PSat} and V_{PDry}) show a moderate negative relationship with porosity (ϕ_{Tot}). (c) S-velocities (V_{S1} and V_{S2} combined) show a weak negative relationship with porosity (ϕ_{Tot}). Seismic velocities of opal and quartz are shown as a reference for linear regressions at zero porosity. (d) P-wave velocity (V_{PDry}) and S-wave velocity (V_{S1} and V_{S2} combined) show a moderate positive linear relationship. (e) Velocity of P-wave (V_{PSat}) and density (ρ), show a moderate positive linear relationship. Error bars are smaller than the plotted symbols.

estimated from our data should be considered as an upper bound on opal-A density.

Primary microbial porosity in sinter produced by gas released by photosynthesis produces bubble-like individual pores in sinter (e.g., Lynne, 2012). Effective medium models for the measured seismic velocity of opal are consistent with moderate aspect ratio (0.2 and 0.8) penny-shaped cracks (Fig. 8c). Thin sections and 3-D analysis of individual pores (Figs. 2,3,4) also show sub-spherical to sub-ellipsoidal shapes.

In Table 2, we compare our results with laboratory measurements on other types of rocks. Quartz sandstone is a sedimentary clastic rock. Primary porosity in sandstone corresponds to the space between grains. For consolidated sandstone, porosity and permeability (Mavko et al., 1998; Bear, 1972, 2012) are lower than sinter. Seismic velocities of sandstone have a wide range (Mavko et al., 1998), and they can be higher than sinter at low porosity. Travertine is an analogue to sinter, but it is formed by precipitation of carbonate from water in low temperature geothermal settings. Images from μX-Ray tomography in travertine (Soete et al., 2015), show a cuboid and rod-like pore shape, while our sinter samples show more spherical to ellipsoidal pores. Furthermore, porosity in travertine is smaller (Table 2), permeability spans a wider range, and seismic velocities are higher than in sinter (Soete et al., 2015; Török and Vásárhelyi, 2010). Opaline chalk is a sedimentary rock composed of biogenetic clasts, siliceous shells of microorganisms that were deposited in the deep ocean. Primary porosity in chalk is given by the space inside of the shells (e.g., Compton, 1991; Chaika and Dvorkin, 1997), thus the total porosity is high, similar to sinter, but the permeability is lower (e.g., Mallon et al., 2005; Fabricius, 2007). Pumice is a vesicular volcanic rock made of volcanic glass containing bubbles. Bubbles in volcanic rocks are formed by the exsolution and expansion of gases. Values of porosity reported in effusive (e.g., Saar and Manga, 1999) and explosive volcanic rocks (Wright et al., 2009; Nguyen et al., 2014) span a wider range than in sinter. Nevertheless the permeability of vesicular volcanic rocks from 10^{-10} to

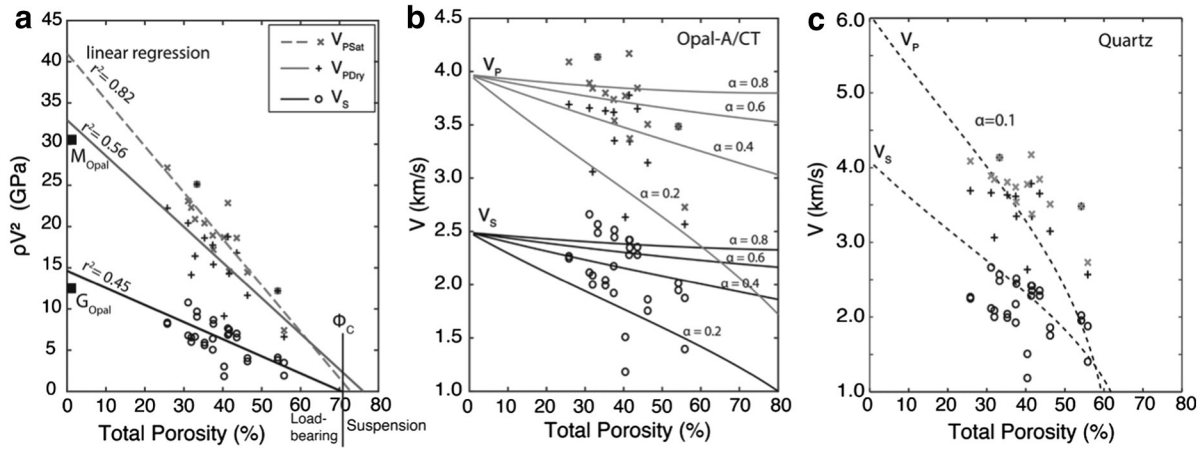

Fig. 8. Critical porosity and effective medium models (Kuster and Toksoz, 1974, Berryman, 1980). (a) Density-velocity (ρV^2) relationship with porosity (ϕ_{Tot}) shows a high positive linear relationship at V_{PSat}, and moderate positive relationship with V_{PDy} and V_S (V_{S1} and V_{S2} combined). The critical porosity of sinter (ϕ_c) occurs when $\rho V_S^2 = 0$, and the shear modulus (G) of the mineral occurs in zero porosity. (b) Kuster-Toksoz effective model for Opal-A/CT for pores of penny-shaped cracks with different aspect ratios 0.2 to 0.8 (same legend as a). (c) Kuster-Toksoz effective model for quartz is consistent only with penny-shaped cracks with aspect ratio of 0.1.

10^{-15} m^2 (e.g., Saar and Manga, 1999; Wright et al., 2009) has a similar range to that of sinter. Seismic velocities of pyroclastic rocks (Vanorio et al., 2002) range within the sinter values.

The permeability (k) of sinter shows a directional dependence with higher values in the direction parallel to the layering than in the orthogonal direction (TAT-006I and TAT-006 M), similar to other layered sedimentary rocks. Values of k can vary by up to 2 orders of magnitude in the same layer (TAT-006 M), reflecting the heterogeneity in individual layers. Field observations suggest higher values of permeability. For example, geysers interact with each other through the subsurface (Rojstaczer et al., 2003), presumably through permeable pathways, requiring an average permeability of the host rock of the order of 10^{-10} m^2 (Munoz-Saez et al., 2015a, 2015b). The permeability measured on centimeter-size cores represents a lower bound on field values, which are likely controlled by fractures, conduits and other high-permeability structures that increase permeability at the field scale.

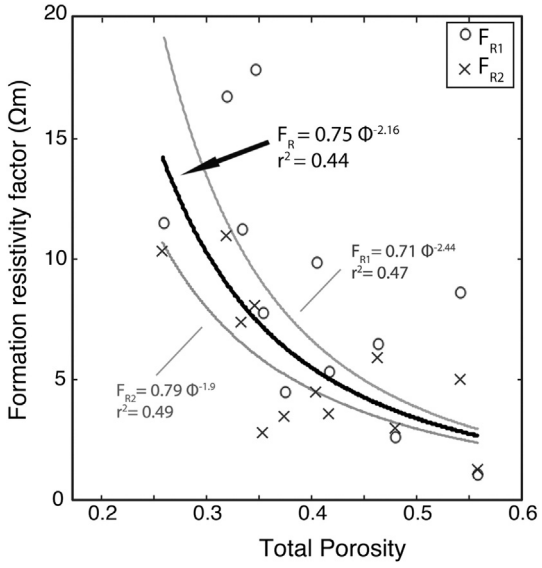

Fig. 9. Formation resistivity factor (F_R) with total porosity (ϕ). F_R shows a moderate power law relationship. For F_{R1} the rocks were saturated with a brine of resistivity $R_{w1} = 41.35$ Ωm. For F_{R2} the resistivity of the brine was $R_{w2} = 15.81$ Ωm. Using all the data m is 2.16 and a is 0.75.

Seismic velocities V_P and V_S varied linearly with porosity (ϕ). Linear regressions of V_P and V_S versus porosity (ϕ) (Fig. 7c) show predictions of seismic velocities at zero porosity that are higher than opal, but less than quartz. Likewise, extrapolating the linear fit of ρV_S^2 to zero porosity we obtained values of G slightly higher than that for opal (Fig. 8a). These results might be due to the high scatter in the seismic velocities. However, accessory minerals can slightly increase density and elastic modulii. From XRD we identify accessory minerals quartz, cristobalite, and zircon. Previous studies in the area also reported trydimite (polymorph of quartz) and halite (Garcia-Valles et al., 2008; Nicolau et al., 2014). In thin sections we find other accessory minerals, including hornblende.

The formation factor shows large scatter (Fig. 9), which can be attributed to heterogeneities in the rock structure. Nevertheless, the cementation exponent m is close to 2, as expected for Archie's Law. The tortuosity factor a depend on the pore structure, grain size, rock texture and compaction of a rock. The value $a = 0.75$ estimated for sinter falls within the expected range of 0.5 to 1.5 (Bassiouni, 1994).

7. Conclusions

To study the petro-physical properties of fine-layered sinters we used multiple approaches (optical microscopy, X-ray diffraction, X-ray computed tomography, and measurements of porosity, permeability, seismic velocity, and electrical resistivity). The physical properties are scattered and empirical relationships have moderate correlation coefficients, as a consequence of heterogeneities between different layers and within single layers.

Sinters are porous rocks, with >90% of their porosity connected. In palisade fabric, the presence of microbial filaments is found to determine pore shape and size distribution. Porosity is higher in fresh samples, decreasing over time as silica precipitates in the pore space, yet preserving the structure seen in the younger, microbial-influenced samples.

Petro-physical properties of sinter depend on lithology and texture. Opal-A is the main phase along with some accessory minerals including quartz, cristobalite, plagioclase, zircon and hornblende. Those accessory minerals, derived from the volcanic country rock, can slightly modify physical properties. Individual pores resemble spherical to elongated bubbles, consistent with effective medium models for the measured seismic velocity of opal containing moderate aspect ratio penny-shaped cracks. Porosity and permeability in sinter are different than clastic sedimentary rocks, and more similar to vesicular volcanic rocks (e.g., pumice). However, permeability shows a directional

Table 2
Petrophysical properties of different rock measured in the laboratory: sinter (this study), consolidate quartz sandstone (Mavko et al., 1998; Bear, 1972, 2012), opaline chalk (Mavko et al., 1998; Chaika and Dvorkin, 1997; Chaika, 1998; Isaacs, 1981; Mallon et al., 2005; Fabricius, 2007), travertine (Mavko et al., 1998; Soete et al., 2015; Török and Vásárhelyi, 2010), pumice (Saar and Manga, 1999; Wright et al., 2009; Nguyen et al., 2014; Vanorio et al., 2002). * Range of permeability includes carbonate chalks.

Rock type	Main mineral	$\rho_{mineral}$ (g/cm^3)	ϕ (%)	ϕ_c (%)	k (m^2)	V_P (km/s)	V_S (km/s)
Sinter	Opal-A	2.18	25–60	71	10^{-12} - 10^{-15}	2.5–4.2	1.0–3.2
Consolidate sandstone	Quartz	2.65	1–40	40	10^{-13} - 10^{-20}	3.0–6.0	1.5–4.0
Opaline Chalk	Opal-A/CT	2.06	10–65	65	10^{-15}- 10^{-22*}	1.2–4.0	0.8–2.2
Tavertine	Calcium carbonate	2.71	5–35	–	10^{-11} - 10^{-18}	3.6–6.0	2.0–3.2
Pumice	Silicate glass	2.4	20–80	80	10^{-10} - 10^{-15}	2.0–3.0	1.0–2.0

dependence with higher values in the direction parallel to the layering than in the orthogonal direction, similar to other layered sedimentary rocks.

For large-scale interpretation of geophysical surveys, and modeling of hydrogeological processes within geysers, our measurements can be considered a lower bound for permeability and resistivity and an upper bound for seismic velocity given that they do not include the effect of fractures and large-scale faulting.

Acknowledgments

This research was supported by: National Science Foundation (EAR1114184), CEGA-University of Chile, Conicyt-Chile, Center for Latin American Studies-University of California Berkeley, and the Judy Webb Chair. We thank people who provided essential help in the laboratory and in the field: Tim Teague, Dula Parkinson, Yuxin Wu, Seiji Nakagawa, Jonathan Ajo-Franklin, Atsuko Namiki, Shaul Hurwitz, Max Rudolph, Angello Negri, Pablo Ortega. We thank the editor and reviewers of JVGR for their valuable comments. The fieldwork was performed with the permission of the Amayras Communities of Caspana and Toconce.

Appendix A

The effective medium model described by Kuster and Toksoz (1974) and Berryman (1980) calculates the effect of the shape of inclusions in a solid on seismic velocities. The general expressions for K_{KT} (bulk modulus) and μ_{KT} (shear modulus) (Kuster and Toksoz, 1974) are:

$$(K_{KT}-K_m)\frac{\left(K_m+\frac{4\mu_m}{3}\right)}{\left(K_{KT}+\frac{4\mu_m}{3}\right)}=\sum_{i=1}^{N}x_i(K_i-K_m)P^{mi} \quad (1)$$

$$(\mu_{KT}-\mu_m)\frac{(\mu_m+\xi_m)}{(\mu_{KT}+\xi_m)}=\sum_{i=1}^{N}x_i(\mu_i-\mu_m)Q^{mi} \quad (2)$$

where, $\xi_m=\frac{\mu_m(9K_m+8\mu_m)}{6(K_m+2\mu_m)}$

The subscripts represent the moduli of inclusion (i) and matrix (m); x_i is the volume of the inclusion (porosity in our case), P^{mi} and Q^{mi} quantify the effect of the inclusions compared to the matrix; there are different expressions for different inclusion shapes.

From Berryman (1980), for penny-shaped cracks, the values of P^{mi} and Q^{mi} are defined as:

$$P^{mi}=\frac{\left(K_m+\frac{4\mu_i}{3}\right)}{\left(K_i+\frac{4\mu_i}{3}+\pi\alpha\beta_m\right)} \quad (3)$$

$$Q^{mi}=\frac{1}{5}\left(1+\frac{8\mu_m}{4\mu_i+\pi\alpha(\mu_m+2\beta_m}+2\frac{K_i+\frac{2(\mu_i+\mu_m)}{3}}{K_i+\frac{4}{3}\mu_i+\pi\alpha\beta_m}\right) \quad (4)$$

where, $\beta_m=\mu_m\left(\frac{3K_m+\mu_m}{3K_m+4\mu_m}\right)$, and α is the aspect ratio (semi-minor axis/semi-major axis) of the inclusion.

The effect on seismic velocities (V_P, V_S),are calculated by inserting the effective moduli into the equations:

$$V_P=\sqrt{\frac{K_{KT}+\frac{4}{3}\mu_{KT}}{\rho}} \quad (5)$$

$$V_S=\sqrt{\frac{\mu_{KT}}{\rho}} \quad (6)$$

To simplify the equations, we considered a single material forming the rock (either opal-A/CT (e.g., Chaika, 1998; Herdianita et al., 2000; Rodgers and Cressey, 2001; Lynne et al., 2008): $\mu_{mOpal}=12.6\times10^9$ Pa, $K_{mOpal}=14.2\times10^9$ Pa, $\rho_{mOpal}=2$ g/cm^3 or quartz (e.g., McSkimin et al., 1965; Mavko et al., 1998): $\mu_{mQz}=44.3\times10^9$ Pa, $K_{mQz}=37.9\times10^9$ Pa, $\rho_{mQz}=2650$ g/cm^3). We used standard values of liquid water for the inclusions ($K_i=2.2\times10^9$ Pa, $\mu_i=0$, and $\rho_i=1$ g/cm^3). α is a free parameter that represents the effective shape of pores in the rock. Although the rock obviously contains many different pore shapes, the effective medium approximation provides a parameterization of the macroscopic behavior of the rock as a whole.

References

Archie, G.E., 1942. Electrical resistivity log as an aid in determining some reservoir characteristics. Trans. AIME 146, 54–61.
Bassiouni, Z., 1994. Theory, measurement, and interpretation of well logs. SPE Textbook Ser. 4.
Bear, J., 1972. Dynamics of Fluids in Porous Media. Elsevier, New York.
Bear, J., 2012. Hydraulics of Groundwater. Courier Corporation.
Benning, L.G., Phoenix, V.R., Yee, N., Konhauser, K.O., 2004. The dynamics of cyanobacterial silicification: an infrared microspectroscopic investigation. Geochim. Cosmochim. Acta 68, 743–757.
Berryman, J.G., 1980. Long-wavelength propagation in composite elastic media II. Ellipsoidal inclusions. J. Acoust. Soc. Am. 68, 1820–1831.
Blank, C.E., Cady, S.L., Pace, N.R., 2002. Microbial composition of near-boiling silicadepositing thermal springs throughout Yellowstone National Park. Appl. Environ. Microbiol. 68, 5123–5135.
Bott, T.L., Brock, T.D., 1969. Bacterial growth rates above 99 °C in Yellowstone hot springs. Science 164, 1411–1412.
Braunstein, D., Lowe, D.R., 2001. Relationship between spring and geyser activity and the deposition and morphology of high temperature (73 °C) siliceous sinter, Yellowstone National Park, Wyoming, U.S.a. J. Sediment. Res. 71, 747–763.
Cady, S.L., 2008. Hyperthermophilic biofilm mineralization; implications for biosignature detection. Geol. Soc. Am. Abstr. Programs 40 (6), 295–296.
Cady, S.L., Farmer, J.D., 1996. Fossilization Processes in Siliceous Thermal Springs: Trends in Preservation along Thermal Gradients. In: Bock, G.R., Goode, G.A. (Eds.), pp. 150–173.
Campbell, K.A., Sannazzaro, K., Rodgers, K.A., Herdianita, N.R., Browne, P.R.L., 2001. Sedimentary facies and mineralogy of the late Pleistocene Umukuri silica sinter, Taupo volcanic zone, New Zealand. J. Sediment. Res. 71, 727–746.
Campbell, K.A., Guido, D.M., Gautret, P., Foucher, F., Ramboz, C., Westall, F., 2015a. Geyserite in hot-spring siliceous sinter: window on earth's hottest terrestrial (paleo) environment and its extreme life. Earth-Sci. Rev. 148, 44–64. http://dx.doi.org/10.1016/j.earscirev.2015.05.009.

Campbell, K.A., Lynne, B.Y., Handley, K.M., Jordan, S., Farmer, J.D., Guido, D.M., Foucher, F., Turner, S., Perry, R.S., 2015b. Tracing biosignature preservation of geothermally silicified microbial textures into the geological record. Astrobiology 15 (10), 858–882.
Cassie, V., 1989. A taxonomic guide to thermally associated algae (excluding diatoms) in New Zealand. Bibl. Phycol. 78, 1–159.
Chaika, C., 1998. Physical Properties and Silica Diagenesis (Ph.D. thesis) Stanford University.
Chaika, C., Dvorkin, J., 1997. Ultrasonic velocities of opaline rocks undergoing silica diagenesis. Geophys. Res. Lett. 24, 2039–2042.
Compton, J.S., 1991. Porosity reduction and burial history of siliceous rocks from the Monterey and Sisquoc formations, point Pedernales area, California. Geol. Soc. Am. Bull. 103 (5), 625–636.
Cortecci, G., Boschetti, T., Mussi, M., Lameli, C.H., Mucchino, C., Barbieri, M., 2005. New chemical and original isotopic data on waters from el Tatio geothermal field, northern Chile. Geochem. J. 39 (6), 547–571.
Cusicanqui, H., Mahon, W.A., Ellis, A.J., 1976. The geochemistry of the El Tatio geothermal field, northern Chile: Second United Nations Geothermal Symposium Proceedings, Lawrence Berkeley Laboratory Univ. of California, Lawrence Berkeley Laboratory, University of California for the United States Energy Research and Development Administration, the United States National Science Foundation, and the United States Geological Survey, Berkeley, California, pp. 140–156.
Fabricius, I.L., 2007. Chalk: composition, diagenesis and physical properties. Geol. Soc. Den. Bull. 55, 97–128.
Fernandez-Turiel, J.L., Garcia-Valles, M., Gimeno-Torrente, D., Saavedra-Alonso, J., Martinez-Manent, S., 2005. The hot spring and geyser sinters of el Tatio, northern Chile. Sediment. Geol. 180, 125–147.
Fournier, R.O., Rowe, J.J., 1966. Estimation of underground temperatures from the silica content of water from hot springs and steam wells. Am. J. Sci. 264, 685–697.
Garcia-Valles, M., Fernandez-Turiel, J.L., Gimeno-Torrente, D., Saavedra-Alonso, J., Martinez-Manet, S., 2008. Mineralogical characterization of silica sinters from the el Tatio geothermal field, Chile. Am. Mineral. 93, 1373–1383.
Giggenbach, W.F., 1978. The isotopic composition of waters from the el Tatio geothermal field, northern Chile. Geochim. Cosmochim. Acta 42, 979–988.
Glennon, J.A., Pfaff, R.M., 2003. The extraordinary thermal activity of el Tatio geyser field, Antofagasta region, Chile. GOSA Trans. 8, 31–78.
Guido, D.M., Campbell, K.A., 2009. Jurassic hot-spring activity in a fluvial setting at La Marciana, Patagonia, Argentina. Geol. Mag. 146, 617–622.
Guido, D.M., Campbell, K.A., 2014. A large and complete Jurassic geothermal field at Claudia, Deseado massif, Santa Cruz, Argentina. J. Volcanol. Geotherm. Res. 275, 61–70.
Guidry, S.A., Chafetz, H.S., 2003. Anatomy of siliceous hot spring examples from Yellowstone National Park, Wyoming, U.S.a. Sediment. Geol. 157, 71–106.
Handley, K.M., Campbell, K.A., Mountain, B.W., Browne, P.R.L., 2005. Abiotic–biotic controls on the origin and development of spicular sinter: in situ growth experiments, champagne pool, Waiotapu, New Zealand. Geobiology 3, 93–114.
Healy, J., 1974. Geological Report on El Tatio Geothermal Field, Antofagasta Province, Chile. UNDP- Report.
Herdianita, N.R., Browne, P.R.L., Rodgers, K.A., Campbell, K.A., 2000. Mineralogical and textural changes accompanying ageing of silica sinter. Mineral. Deposita 35, 48–62.
Hinman, N.W., Lindstrom, R.F., 1996. Seasonal changes in silica deposition in hot spring systems. Chem. Geol. 132, 237–246.
Huber, R., Eder, W., Heldwein, S., Wanner, G., Huber, H., Rachel, R., Stetter, K.O., 1998. Thermocrinis ruber, gen. Nov., sp. nov., a pink-filament-forming hyperthermophilic bacterium isolated from Yellowstone national park. Appl. Environ. Microbiol. 64, 3576–3583.
Isaacs, C.M., 1981. Porosity Reduction during Diagenesis of the Monterey Formation, Santa Barbara Coastal Area, California. In: Garrison, R.E., Douglas, R.G. (Eds.), The Monterey Formation and Related Siliceous Rocks of California. Society of Economic Paleontologists and Mineralogists, Los Angeles, Pacific Section, pp. 257–271.
Jones, B., Renaut, R.W., 1996. Influence of thermophilic bacteria on calcite and silica precipitation in hot springs with water temperatures above 90 °C; evidence from Kenya and New Zealand. Can. J. Earth Sci. 32, 72–83.
Jones, B., Renaut, R.W., 1997. Formation of silica oncoids around geysers and hot springs at el Tatio, northern Chile. Sedimentology 44, 287–304.
Jones, B., Renaut, R.W., 2004. Water content of opal-a: implications for the origin of laminae in geyserite and sinter. J. Sediment. Res. 74, 117–128.
Jones, B., Renaut, R.W., Rosen, M.R., 2000. Stromatolites forming in acidic hot-spring waters, North Island, New Zealand. PALAIOS 15, 450–475.
Jones, B., Renaut, R.W., Rosen, M.R., 2003. Silicified microbes in a geyser mound: the enigma of low-temperature cyanobacteria in a high-temperature setting. PALAIOS 18, 87–109.
Konhauser, K.O., Ferris, F.G., 1996. Diversity of iron and silica precipitation by microbial mats in hydrothermal waters, Iceland: implications for Precambrian iron formations. Geology 24, 323–326.
Konhauser, K.O., Phoenix, V.R., Bottrell, S.H., Adams, D.G., Head, I.M., 2001. Microbial–silica interactions in modern hot spring sinter: possible analogues for some Precambrian siliceous stromatolites. Sedimentology 48, 415–433.
Konhauser, K.O., Jones, B., Reysenbach, A., Renaut, R.W., 2003. Hot spring sinters: keys to understanding Earth's earliest life forms. Can. J. Earth Sci. 40, 1713–1724.
Kuster, G.T., Toksoz, M.N., 1974. Velocity and attenuation of seismic waves in two-phase media. Part I. Theoretical formulations. Geophysics 39, 587–606.
Lahsen, A., 1976a. La actividad geotermal y sus relaciones con la tectónica y el volcanismo en el norte de Chile. I Congreso Geológico Chileno, Actas B105–B127 Universidad de Chile / Publisher: Universidad de Chile.
Lahsen, A., 1976b. Geothermal exploration in Northern Chile–Summary. Circum-Pacific Energy and Mineral Resources Conference, Hawaii. The American Association of Petroleum Geologists, Memoir 25, 169–175.
Lahsen, A., Trujillo, P., 1975. El Tatio Geothermal Field. Proc. of the Second United Nations Symposium on the Development and Use of Geothermal Resources. San Francisco, California, pp. 157–178 (May 20–29, 1975).
Lowe, D.R., Anderson, K.S., Braunstein, D., 2001. The Zonation and Structuring of Siliceous Sinter around Hot Springs, Yellowstone National Park, and the Role of Thermophilic Bacteria in its Deposition. In: Reysenbach, A.M., Voytech, M., Mancinelli, R. (Eds.), Thermophiles: Biodiversity. Ecology and Evolution. Kluwer Academic/Plenum Publishers, New York, pp. 143–166.
Lynne, B.Y., 2012. Mapping vent to distal-apron hot spring paleo-flow pathways using siliceous sinter architecture. Geothermics 43, 3–24.
Lynne, B.Y., Campbell, K.A., 2003. Diagenetic transformations (opal-a to quartz) of low- and mid-temperature microbial textures in siliceous hot-spring deposits, Taupo volcanic zone, New Zealand. Can. J. Earth Sci. 40, 1679–1696.
Lynne, B.Y., Campbell, K.A., Moore, J., Browne, P.R.L., 2005. Diagenesis of 1900-year-old siliceous sinter (opal-a to quartz) at opal mound, Roosevelt Hot Springs, Utah, U.S.a. Sediment. Geol. 119, 249–278.
Lynne, B.Y., Campbell, K.A., Moore, J.N., Browne, P.R.L., 2008. Origin and evolution of the Steamboat Springs siliceous sinter deposit, Nevada, U.S.a. Sediment. Geol. 210, 111–131.
Lynne, B.Y., Morata, D., Reich, M., 2012. High versus low altitude hot spring settings and associated sinter textures from el Tatio, Chile, and the Taupo volcanic zone, New Zealand. Geotherm. Res. Coun. Trans. 36, 925–929.
Mallon, A.J., Swarbrick, R.E., Katsube, T.J., 2005. Permeability of fine-grained rocks: new evidence from chalks. Geology 33 (1), 21–24.
Mavko, G., Mukerji, T., Dvorkin, J., 1998. The Rock Physics Handbook: Tools for Seismic Analysis in Porous Media. Cambridge University Press.
McSkimin, H.J., Andreatch Jr., P., Thurston, R., 1965. Elastic moduli of quartz versus hydrostatic pressure at 25 and − 195.8C. J. Appl. Phys. 36 (5), 1624–1632.
Mountain, B.W., Benning, L.G., Boerema, J.A., 2003. Experimental studies on New Zealand hot spring sinters: rates of growth and textural development. Can. J. Earth Sci. 40, 1643–1667.
Munoz-Saez, C., Manga, M., Hurwitz, S., Rudolph, M., Namiki, A., Wang, C.-Y., 2015a. Dynamics within geyser conduits, and sensitivity to environmental perturbations: insights froma periodic geyser in the el Tatio geyser field, Atacama Desert, Chile. J. Volcanol. Geotherm. Res. 292, 41–55. http://dx.doi.org/10.1016/j.jvolgeores.2015.01.002.
Munoz-Saez, C., Namiki, A., Manga, M., 2015b. Geyser eruption intervals and interactions: examples from el Tatio, Atacama, Chile. J. Geophys. Res. 120. http://dx.doi.org/10.1002/2015JB012364.
Nguyen, C.T., Gonnermann, H.M., Houghton, B.F., 2014. Explosive to effusive transition during the largest volcanic eruption of the 20th century (Novarupta 1912, Alaska). Geology 42 (8), 703–706.
Nicolau, C., Reich, M., Lynne, B., 2014. Physico-chemical and environmental controls on siliceous sinter formation at the high-altitude el Tatio geothermal field, Chile. J. Volcanol. Geotherm. Res. 282, 60–76. http://dx.doi.org/10.1016/j.jvolgeores.2014.06.012.
Nur, A., Marion, D., Yin, H., 1991. Wave Velocities in Sediments. In: Hovem, J., Richardson, M.D., Stoll, R.D. (Eds.), Shear Waves in Marine Sediments. Kluwer Academic, pp. 131–140.
Nur, A., Mavko, G., Dvorkin, J., Galmundi, D., 1995. Critical Porosity: The Key to Relating Physical Properties to Porosity in Rocks. Proc. 65th Ann Int. Meeting Soc. Expl. Geophys. 878
Nur, A., Mavko, G., Dvorkin, J., Galmudi, D., 1998. Critical porosity: a key to relating physical properties to porosity in rocks. Lead. Edge 17 (3), 357–362.
O'Connell, R.J., Budiansky, B., 1974. Seismic velocities in dry and saturated cracked solids. J. Geophys. Res. 79 (35), 5412–5426. http://dx.doi.org/10.1029/JB079i035p05412.
Phoenix, V.R., Bennett, P.C., Engel, A.S., Tyler, S.W., Ferris, F.G., 2006. Chilean high-altitude hot-spring sinters: a model system for UV screening mechanisms by early Precambrian cyanobacteria. Geobiology 4, 15–28. http://dx.doi.org/10.1111/j.1472-4669.2006.00063.x.
Pierson, B.K., Castenholz, R.W., 1974. A phototrophic gliding filamentous bacterium of hot springs, Chloroflexus aurantiacus. Arch. Microbiol. 100, 5–24.
Renaut, R.W., Jones, B., Le Turdu, C., 1999. Calcite lilypads and ledges at Lorusio Hot Springs, Kenya Rift Valley: travertine precipitation at the air–water interface. Can. J. Earth Sci. 36, 649–666.
Rice, C.M., Trewin, N.H., Anderson, L.I., 2002. Geological setting of the early Devonian Rhynie cherts, Aberdeenshire, Scotland: an early terrestrial hot-spring system. J. Geol. Soc. Lond. 159, 203–214.
Rodgers, K.A., Cressey, G., 2001. The occurrence, detection and significance of moganite (SiO_2) among some silica sinters. Mineral. Mag. 65, 157–167.
Rodgers, K.A., Greatrex, R., Hyland, M., Simmons, S.F., Browne, P.R.L., 2002. A modern evaporitic occurrence of teruggite, $Ca_4MgB_{12}As2O_{28} \cdot 18H_2O$, and nobleite, $CaB_6O_{10} \cdot 4H_2O$, from the el Tatio geothermal field, Antofagasta Province, Chile. Mineral. Mag. 66, 253–259.
Rodgers, K.A., Browne, P.R.L., Buddle, T.F., Cook, K.L., Greatrex, R.A., Hampton, W.A., Herdianita, N.R., Holland, G.R., Lynne, B.Y., Martin, R., Newton, Z., Pastars, D., Sannazarro, K.L., Teece, C.I.A., 2004. Silica phases in sinters and residues from geothermal fields of New Zealand. Earth-Sci. Rev. 66, 1–61.
Rojstaczer, S., Galloway, D.L., Ingebritsen, S.E., Rubin, D.M., 2003. Variability in geyser eruptive timing and its causes: Yellowstone National Park. Geophys. Res. Lett. 30 (18), 1953. http://dx.doi.org/10.1029/2003GL017853.
Ruff, S.W., Farmer, J.D., Calvin, W.M., Herkenhoff, K.E., Johnson, J.R., 2011. Characteristics, distribution, origin, and significance of opaline silica observed by the Spirit rover in Gusev crater, Mars. J. Geophys. Res. 116, E00F23. http://dx.doi.org/10.1029/2010JE003767.
Saar, M.O., Manga, M., 1999. Permeability of vesicular basalts. Geophys. Res. Lett. 26, 111–114. http://dx.doi.org/10.1029/1998GL900256 (issn: 0094–8276).
Schinteie, R., Campbell, K.A., Browne, P.R.L., 2007. Microfacies of stromatolitic sinter from acid–sulphate–chloride springs at Parariki stream, Rotokawa geothermal field, New Zealand. Palaeontol. Electron. 10 (1), 1–33 (4A, http://palaeo-electronica.org/paleo/2007_1/sinter/index.html).
Sillitoe, R.H., 1993. Epithermal Models: Genetic Types, Geometrical Controls and Shallow Features. In: Kirkham, R.V., Sinclair, W.D., Thorpe, R.I., Duke, J.M. (Eds.), Mineral Deposits Modeling: Special Paper of the Geological Association of Canada. 40, pp. 403–417.
Sillitoe, R.H., 2015. Epithermal paleosurfaces. Mineral. Deposita 50 (7), 767–779. http://dx.doi.org/10.1007/s00126-015-0614-z.
Soete, J., Kleipool, L.M., Claes, H., Claes, S., Hamaekers, H., Kele, S., Özkul, M., Foubert, A., Reijmer, J.J.G., Swennen, R., 2015. Acoustic properties in travertines and their relation to porosity and pore types. Mar. Pet. Geol. 59, 320–335. http://dx.doi.org/10.1016/j.marpetgeo.2014.09.004.
Squyres, S.W., Arvidson, R.E., Ruff, S., Gellert, R., Morris, R.V., Ming, D.W., Crumpler, L., Farmer, J.D., Des Marais, D.J., Yen, A., McLennan, S.M., Calvin, W., Bell, J.F., Clark, B.C., Wang, A., McCoy, T.J., Schmidt, M.E., DeSouza Jr., P.A., 2008. Detection of silica-rich deposits on Mars. Science 320 (5879), 1063–1067.

Tassi, F., Aguilera, F., Darrah, T., Vaselli, O., Capaccioni, B., Poreda, R.J., Delgado Huertas, A., 2010. Fluid geochemistry of hydrothermal systems in the Arica-Parinacota, Tarapacá and Antofagasta regions (northern Chile). J. Volcanol. Geotherm. Res. 192, 1–15.

Török, Á., Vásárhelyi, B., 2010. The influence of fabric and water content on selected rock mechanical parameters of travertine, examples from Hungary. Eng. Geol. 115 (3), 237–245.

Vanorio, T., Prasad, M., Patella, D., Nur, A., 2002. Ultrasonic velocity measurements in volcanic rocks: correlation with microtexture. Geophys. J. Int. 149 (1), 22–36.

Walter, M.R., 1972. A hot spring analog for the depositional environment of Precambrian iron formations of the Lake superior region. Econ. Geol. 67, 965–980.

Walter, M.R., 1976a. Geyserites of Yellowstone National Park: An Example of Abiogenic "Stromatolites". In: Walter, M.R. (Ed.), Stromatolites. Elsevier, Amsterdam, pp. 87–112.

Walter, M.R., 1976b. Hot-Spring Sediments in Yellowstone National Park. In: Walter, M.R. (Ed.), Stromatolites. Elsevier, Amsterdam, pp. 489–498.

Walter, M.R., Des Marais, D., Farmer, J.D., Hinman, N.W., 1996. Lithofacies and biofacies of mid-Paleozoic thermal spring deposits in the Drummond Basin, Queensland, Australia. PALAIOS 11, 497–518.

Watanabe, M.M., Kurogi, M., 1975. Taxonomic *Calothrix scopulorum* and *C. crustacea*. Bot. Mag. Tokyo 88, 111–125.

Weed, W.H., 1889. On the formation of siliceous sinter by the vegetation of thermal springs. Am. J. Sci. 37, 351–359.

Westall, F., Boni, L., Guerzoni, E., 1995. The experimental silicificationof microorganisms. Palaeontology 38 (3), 495–528.

Westall, F., Steele, A., Toporski, J., Walsh, M., Allen, C., Guidry, S., McKay, D., Chafetz, H., 2000. Polymeric substances and biofilms as biomarkers in terrestrial materials: implications for extraterrestrial samples. J. Geophys. Res. 105 (E10), 24,511–24,527.

Westall, F., Campbell, K.A., Breheret, J.G., Foucher, F., Gautret, P., Hubert, A., Souriel, S., Grassineau, N., Guido, D.M., 2015. Archean (3.3 Ga) microbe-sediment systems were diverse and flourished in a hydrothermal context. Geology http://dx.doi.org/10.1130/G36646.1.

White, D.E., Thompson, G.A., Sandberg, C.H., 1964. Rocks, structure, and geologic history of Steamboat Springs thermal area, Washoe County, Nevada. U. S. Geol. Surv. Prof. Pap. 458-B (63 pp.).

Wright, H.M., Cashman, K.V., Gottesfeld, E.H., Roberts, J.J., 2009. Pore structure of volcanic clasts: measurements of permeability and electrical conductivity. Earth Planet. Sci. Lett. 280 (1), 93–104.

Yee, N., Phoenix, V.R., Konhauser, K.O., Benning, L.G., Ferris, F.G., 2003. The effect of cyanobacteria on silica precipitation at neutral pH: implications for bacterial silicification in geothermal hot springs. Chem. Geol. 199, 83–90.